



NAVAL POSTGRADUATE SCHOOL

MONTEREY, CALIFORNIA

THESIS

**OPTICAL CORRECTION OF SPACE-BASED
TELESCOPES USING A DEFORMABLE MIRROR
SYSTEM**

by

Mark C. Mueller

December 2016

Co-Advisors:

Brij Agrawal
Jae Jun Kim

Approved for public release. Distribution is unlimited.

THIS PAGE INTENTIONALLY LEFT BLANK

| | | | | |
|--|---|--|---|--|
| REPORT DOCUMENTATION PAGE | | | <i>Form Approved OMB No. 0704-0188</i> | |
| Public reporting burden for this collection of information is estimated to average 1 hour per response, including the time for reviewing instruction, searching existing data sources, gathering and maintaining the data needed, and completing and reviewing the collection of information. Send comments regarding this burden estimate or any other aspect of this collection of information, including suggestions for reducing this burden, to Washington headquarters Services, Directorate for Information Operations and Reports, 1215 Jefferson Davis Highway, Suite 1204, Arlington, VA 22202-4302, and to the Office of Management and Budget, Paperwork Reduction Project (0704-0188) Washington, DC 20503. | | | | |
| 1. AGENCY USE ONLY (Leave blank) | 2. REPORT DATE December 2016 | 3. REPORT TYPE AND DATES COVERED Master's thesis | | |
| 4. TITLE AND SUBTITLE OPTICAL CORRECTION OF SPACE-BASED TELESCOPES USING A DEFORMABLE MIRROR SYSTEM | | | 5. FUNDING NUMBERS | |
| 6. AUTHOR(S) Mark C. Mueller | | | | |
| 7. PERFORMING ORGANIZATION NAME(S) AND ADDRESS(ES) Naval Postgraduate School Monterey, CA 93943-5000 | | | 8. PERFORMING ORGANIZATION REPORT NUMBER | |
| 9. SPONSORING /MONITORING AGENCY NAME(S) AND ADDRESS(ES) | | | 10. SPONSORING / MONITORING AGENCY REPORT NUMBER | |
| 11. SUPPLEMENTARY NOTES The views expressed in this thesis are those of the author and do not reflect the official policy or position of the Department of Defense or the U.S. Government. IRB Protocol number ____N/A____. | | | | |
| 12a. DISTRIBUTION / AVAILABILITY STATEMENT Approved for public release. Distribution is unlimited. | | | 12b. DISTRIBUTION CODE | |
| 13. ABSTRACT (maximum 200 words) Adaptive optics offer the potential to reduce the high cost and long lead time associated with manufacturing mirrors for spaced-based telescopes by allowing lighter materials to be substituted. These lighter materials lack the optical performance of traditional space-based mirrors. Deformable mirrors could be used to correct for surface aberrations in order to improve the optical quality by altering their surface to adjust the wavefront. Research focused on placing a deformable mirror at the exit pupil of a simulated telescope. Experimental work first studied a severely degraded one-meter carbon fiber reinforced polymer mirror to establish a baseline. Simulations were conducted to see how a notional deformable mirror would be able to negate the optical effects due to a distorted mirror in combination with field angle effects. Results from the investigation showed that a deformable mirror yielded the greatest benefit when applied to a distorted mirror surface. Increasing the actuator count on the deformable mirror boosted the root mean square performance across all field angles. Increasing the actuator stroke yielded minimal benefits after a certain reduction in wavefront had already been achieved. Further research is recommended to focus on using a continuous deformable mirror to account for field angle effects. | | | | |
| 14. SUBJECT TERMS adaptive optics, deformable mirror | | | 15. NUMBER OF PAGES 59 | |
| | | | 16. PRICE CODE | |
| 17. SECURITY CLASSIFICATION OF REPORT Unclassified | 18. SECURITY CLASSIFICATION OF THIS PAGE Unclassified | 19. SECURITY CLASSIFICATION OF ABSTRACT Unclassified | 20. LIMITATION OF ABSTRACT UU | |

THIS PAGE INTENTIONALLY LEFT BLANK

Approved for public release. Distribution is unlimited.

**OPTICAL CORRECTION OF SPACE-BASED TELESCOPES USING A
DEFORMABLE MIRROR SYSTEM**

Mark C. Mueller
Lieutenant, United States Navy
B.S., United States Naval Academy, 2010

Submitted in partial fulfillment of the
requirements for the degree of

MASTER OF SCIENCE IN ASTRONAUTICAL ENGINEERING

from the

**NAVAL POSTGRADUATE SCHOOL
December 2016**

Approved by: Brij Agrawal
 Co-Advisor

Jae Jun Kim
Co-Advisor

Garth Hobson
Chair, Department of Mechanical and Aerospace Engineering

THIS PAGE INTENTIONALLY LEFT BLANK

ABSTRACT

Adaptive optics offer the potential to reduce the high cost and long lead time associated with manufacturing mirrors for spaced-based telescopes by allowing lighter materials to be substituted. These lighter materials lack the optical performance of traditional space-based mirrors. Deformable mirrors could be used to correct for surface aberrations in order to improve the optical quality by altering their surface to adjust the wavefront.

Research focused on placing a deformable mirror at the exit pupil of a simulated telescope. Experimental work first studied a severely degraded one-meter carbon fiber reinforced polymer mirror to establish a baseline. Simulations were conducted to see how a notional deformable mirror would be able to negate the optical effects due to a distorted mirror in combination with field angle effects.

Results from the investigation showed that a deformable mirror yielded the greatest benefit when applied to a distorted mirror surface. Increasing the actuator count on the deformable mirror boosted the root mean square performance across all field angles. Increasing the actuator stroke yielded minimal benefits after a certain reduction in wavefront had already been achieved. Further research is recommended to focus on using a continuous deformable mirror to account for field angle effects.

THIS PAGE INTENTIONALLY LEFT BLANK

TABLE OF CONTENTS

| | | |
|------|--|----|
| I. | INTRODUCTION..... | 1 |
| A. | PURPOSE..... | 1 |
| B. | OVERVIEW | 1 |
| II. | SPACE-BASED TELESCOPE DESIGN CONSIDERATIONS..... | 3 |
| A. | ADAPTIVE OPTICS..... | 3 |
| B. | DESIGN CONSTRAINTS | 3 |
| C. | OPTICAL CONSIDERATIONS..... | 4 |
| D. | DESIGN | 5 |
| E. | ENVIRONMENTAL CONSIDERATIONS..... | 8 |
| F. | OPTICAL SOURCES OF ERROR | 10 |
| G. | WAVEFRONT ERROR..... | 11 |
| H. | FIELD ANGLE MAGNIFICATION..... | 11 |
| III. | EXPERIMENTAL SETUP | 13 |
| A. | CFRP CORRECTION | 13 |
| B. | DEFORMABLE MIRROR..... | 15 |
| C. | WAVEFRONT SENSING | 16 |
| D. | CONTROL | 17 |
| IV. | NOTIONAL TELESCOPE DESIGN AND CORRECTION | 21 |
| A. | TELESCOPE DESIGN | 21 |
| B. | FIELD ANGLE CONSIDERATIONS..... | 25 |
| C. | ZERNIKE POLYNOMIALS..... | 26 |
| V. | FUTURE WORK AND CONCLUSION | 37 |
| A. | CONCLUSION | 37 |
| B. | SUITABILITY OF MEMS IN THE SPACE ENVIRONMENT | 37 |
| C. | CONTINUOUS FACE SHEET MEMS DEVICE | 37 |
| D. | OFF AXIS TESTING | 38 |
| | APPENDIX. CONTROL SCRIPT | 39 |
| | LIST OF REFERENCES..... | 43 |
| | INITIAL DISTRIBUTION LIST | 45 |

THIS PAGE INTENTIONALLY LEFT BLANK

LIST OF FIGURES

| | | |
|------------|--|----|
| Figure 1. | Field of Regard and View for the SMT. Source: [9]. | 5 |
| Figure 2. | Ray Trace Diagrams for a One- (a), Two- (b), and Three-Mirror Telescope (c). Adapted from [6]. | 6 |
| Figure 3. | Two-Mirror Conic Surface Design Options. Source: [10]. | 7 |
| Figure 4. | Key Properties for a Selection of Optical Remote Sensing Satellites. Source: [11]. | 8 |
| Figure 5. | The Five Primary Optical Aberrations. Source: [10]. | 10 |
| Figure 6. | One-Meter NPS CRP Mirror | 13 |
| Figure 7. | NPS CFRP One-Meter Mirror Interferometric Measurement | 14 |
| Figure 8. | Experimental Optical Schematic for the CFRP Mirror Correction | 15 |
| Figure 9. | Boston 492-DM as Shown in the Optical Schematic from Figure 8 | 16 |
| Figure 10. | Screenshot from the MetroPro Software. | 17 |
| Figure 11. | Simulink Integral Gain Controller. | 17 |
| Figure 12. | Before (a) and After (b) CFRP Mirror Correction by the Boston 492-DM | 18 |
| Figure 13. | 2D (a) and 3D (b) Wavefront of Segmented Boston 492 DM. Source: [14]. | 19 |
| Figure 14. | Optical Layout of the SMT. Source: [9]. | 21 |
| Figure 15. | Zmax Ray Trace Diagram for Notional Telescope | 22 |
| Figure 16. | Experimental (a) and Model Results (b) of a Continuous DM. Source: [14]. | 24 |
| Figure 17. | 3D (a) and 2D (b) Surface Plots of Actuator 24 | 24 |
| Figure 18. | 2D (a) and 3D (b) Raw Wavefront Portion of CFRP Mirror | 27 |
| Figure 19. | 2D (a) and 3D (b) Fitted Wavefront Portion of CFRP Mirror | 28 |
| Figure 20. | Perfect Primary Mirror Comparison of Variables | 31 |
| Figure 21. | Distorted Primary Mirror Comparison of Variables | 32 |
| Figure 22. | Bar Chart Comparing Variables to RMS | 33 |
| Figure 23. | Zmax Ray Trace Diagram for Notional Telescope with a Magnification Factor of 100 | 34 |
| Figure 24. | Perfect Primary Mirror Comparison of Variables with a Magnification Factor of 100 | 35 |
| Figure 25. | Distorted Primary Mirror Comparison of Variables with a Magnification Factor of 100 | 36 |

THIS PAGE INTENTIONALLY LEFT BLANK

LIST OF TABLES

| | | |
|----------|--|----|
| Table 1. | Table of Results for Field Angle Only Correction..... | 26 |
| Table 2. | Table of CFRP Zernike Coefficients | 28 |
| Table 3. | Table of Results for Field Angle and Primary Mirror Correction. | 29 |
| Table 4. | Comparison of 100 versus 361 Actuator DM for Varying Strokes. | 30 |

THIS PAGE INTENTIONALLY LEFT BLANK

I. INTRODUCTION

In an age of decreasing budgets and rapidly developing technologies, the United States can maintain strategic and operational advantages in space through production of cheaper and more capable satellites by innovative means. One such method is the use of adaptive optics in spaced-based telescopes.

A. PURPOSE

Issues of cost and weight currently face high-resolution electro-optical (EO) satellites as remote sensing vehicles attempt to image the Earth in increasing detail. Both of these issues are directly related to the primary mirror. A way to reduce both factors is by introducing lightweight materials for use as primary mirrors. The principal issue with these lighter mirrors is that they lack the optical performance of the monolithic glass mirrors currently in use. Placing deformable mirrors (DM) in the optics' path would allow for corrections to the wavefront required by these less-than-perfect lighter mirrors. By exploring the possibility of placing a DM in the aft portion of an optical telescope, this thesis will examine the associated design considerations and effects on performance. To accomplish this, design factors for an optical telescope will first be outlined. A baseline for a degraded mirror will be established by taking measurements from a damaged carbon fiber reinforced polymer (CFRP) mirror. Finally, a theoretical telescope will be modeled with both a perfect primary and distorted mirror for an optical layout that has the DM at the exit pupil location. At this location, the DM will attempt to correct the wavefront for both aberration and field angle effects.

B. OVERVIEW

In addition to the technological challenges of placing large-aperture telescopes in space, the Department of Defense (DOD) and the Intelligence Community face cost constraints. The National Security Space Strategy seeks to promote a robust space capability that is consistent with defense objectives and is affordable to the DOD [1]. Currently, heavy, finely polished monolithic mirrors are manufactured over several years before being integrated into an EO satellite. The primary mirrors are not only heavy, but

also expensive. Additionally, the mirrors require a long lead time to manufacture. The aperture of a telescope directly affects parameters such as angular resolution and sensitivity [2]. Thus, larger mirrors are desired in order to have increased resolution. These larger mirrors not only present cost and weight issues themselves, but also impose constraints on the launch vehicle, which must have fairings that can accommodate their size. Researchers have been pursuing low-density materials for use as primary mirrors in order to negate these undesired effects. However, these lighter materials are more susceptible to thermal, vibrational, gravitational, and alignment issues [3]. If these lighter materials are to be used they will require a means to correct for their distortions. The use of adaptive optics is one such means to correct for these errors.

This project is part of a much larger investigation involving various configurations utilizing adaptive optics to correct for imperfections in the primary mirror of space-based telescopes. Previous work examined a woofer-tweeter configuration in which actuators were embedded in the primary mirror to make them actively controlled for wavefront correction. A piezoelectric DM has also been placed in the optical path of a passive primary mirror in another attempt to correct the wavefront. This thesis seeks to look at a lightweight passive primary mirror scenario in which a DM is placed at the exit pupil to overcome not just wavefront errors caused by the lighter materials, but also affects from field angle magnification.

II. SPACE-BASED TELESCOPE DESIGN CONSIDERATIONS

A. ADAPTIVE OPTICS

Adaptive optics is a system that can improve the optical performance of a wavefront by sensing wavefront distortions and correcting them through the use of a deformable mirror (DM). A DM is a device which can distort its surface in order to compensate for various aberrations by pushing or pulling actuators located behind the optical surface [4]. Examples of aberrations include external sources such as atmospheric effects and imperfections on the surface of the mirror. Key metrics of a deformable mirror include aperture size, actuator stroke length, number of actuators, and response time.

The benefits of applying adaptive optics to space-based applications is that the heavy, highly-polished mirrors would no longer need to be just that, a high quality piece of glass. Instead, different and lighter weight materials, such as a CFRP mirror, could be used as substitutes. A mirror made of finely polished glass would be replaced by a mirror that has some imperfections that cause distortions to the wavefront but are corrected for by a DM.

B. DESIGN CONSTRAINTS

The first task in designing an EO telescope is identifying the requirements. These factors include the desired target of interest, preferred resolution, expected brightness of the target, and wavelengths of interest. The wavelength can encompass a broad spectral range from the visible spectrum to the near infrared [5]. Once these parameters have been determined, requirements for power, structure, thermal, propulsion, communication, guidance, and navigation and control can be calculated. Finally, the satellite must be able to fit inside the launch vehicle and meet mass and volume constraints.

C. OPTICAL CONSIDERATIONS

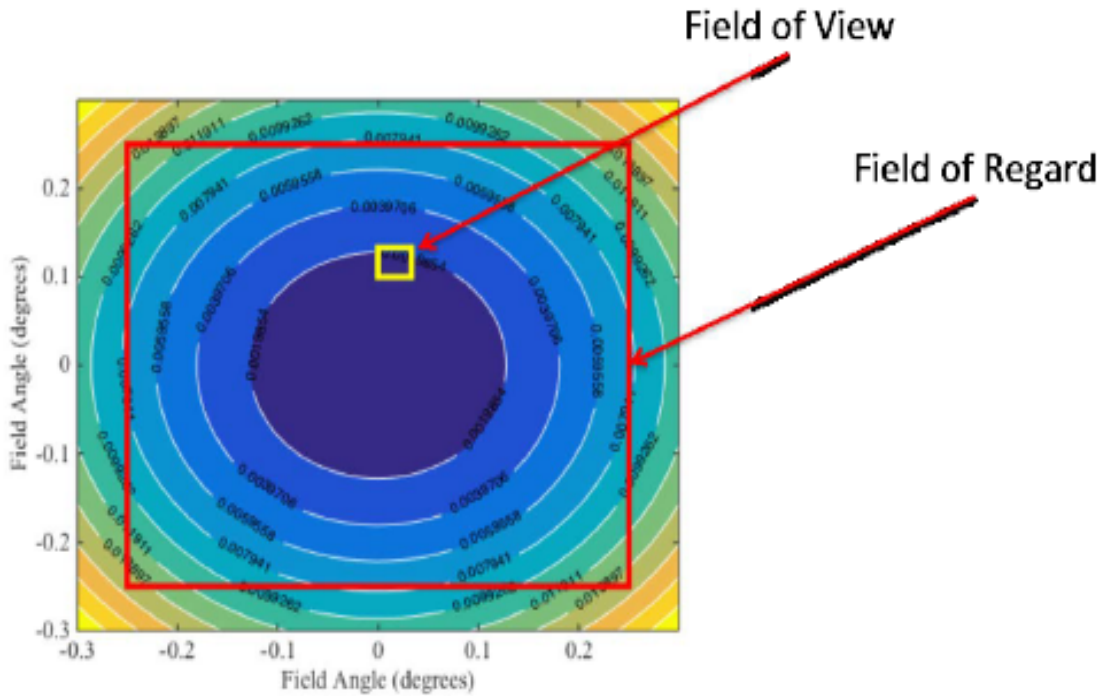
When designing optics for space-based telescopes the natural starting point is the optical path. Considerations include the field of view (FOV), the diffraction-limited wavelength, the sensitivity, and the image quality [6]. Typically, remote-sensing satellites are placed in low earth orbit (LEO). This environment presents thermal swing challenges as the vehicle goes in and out of eclipse. As the space vehicle goes in and out of the Earth's shadow materials will expand and contract.

One of the first parameters determined is the size of the primary mirror. For monolithic mirrors, the typical cutoff size is approximately three meters so that the satellite is able to fit in the shroud of the launch vehicle [6]. Additionally, the primary mirror makes up a significant portion of the weight of the satellite. For example, the Hubble Space Telescope (HST) used ultra-low expansion (ULE) glass for its 2.4 meter primary mirror. While ULE glass has excellent optical qualities, its high-area density of 180 kg/m^2 makes it exceptionally heavy [7]. The weight also makes increasing the diameter of the primary mirror a challenging structural problem for the spacecraft in addition to fitting inside of a launch vehicle. In contrast, the beryllium mirrors on the James Webb Space Telescope (JWST) have an areal density of 13 kg/m^2 . However, these mirrors took many more years to build than those of HST and are much more expensive than HST's primary mirror [8].

Exposure time is inversely proportional to the area of the aperture in addition to the intensity of the incoming light and the sensitivity of the detector. Lenses and/or additional mirrors can be used to focus light rays in order to artificially create the effects of having a larger aperture. However, lenses only work when looking on axis. Wide field of view (WFOV) systems, such as remote-sensing telescopes, require complex lens configurations so the system can image off axis.

The segmented mirror telescope (SMT) located at the Naval Postgraduate School (NPS) is a technology demonstrator for a segmented space-based telescope. The field of regard (FOR) is the total possible area that could be imaged by the telescope at any given moment. The FOV is the area that can be imaged by the focal plane array (FPA). A fast

steering mirror is used to move the FOV within the FOR so that the spacecraft does not need to physically move to a new target as long as it is within the FOR. This is known as field angle steering. The difference between FOR and FOV for SMT is shown in Figure 1.



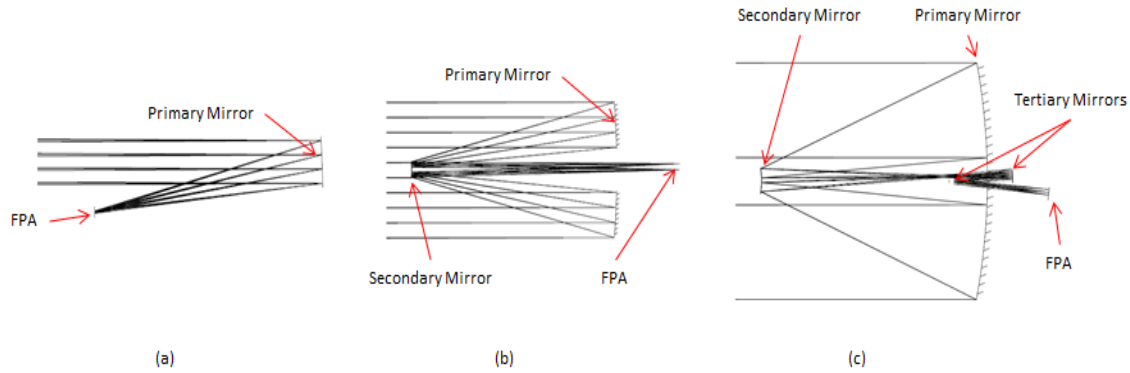
Allen [9] showed on the segmented telescope that as the FOV moves further away from being on axis, represented by the central purple circle, effects of field magnification start come into play. These magnification effects are denoted by the concentric rings of various colors representing specific magnification values as shown in the contours of the plot and are a result of path length error.

Figure 1. Field of Regard and View for the SMT. Source: [9].

D. DESIGN

Mirror configurations include using one or multiple mirrors to relay light. A multi-mirror option is preferable as additional mirrors help correct for increasing orders of aberrations. For example, a two-mirror arrangement was used in HST to avoid the effects of spherical aberrations and coma. Similarly, JWST used a three-mirror system to correct for spherical aberrations, coma, and astigmatism. In a three-mirror system, the

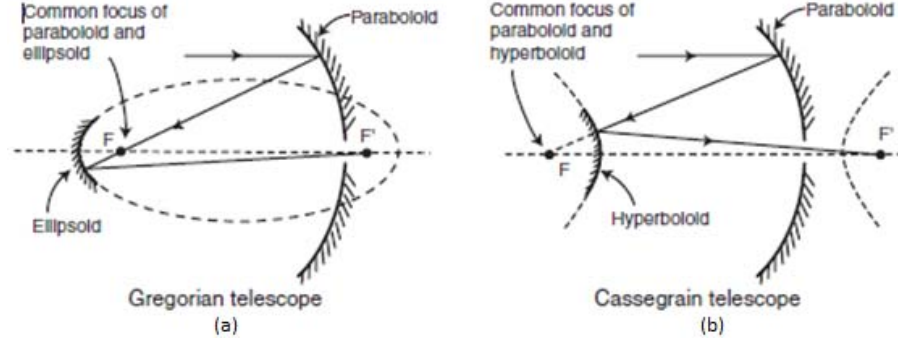
first mirror is the primary mirror, the second is the secondary mirror, and the third is the tertiary mirror. Figure 2 is a depiction of how one-, two-, and three-mirror systems could be configured.



From Feinbert et al. [6], ray trace diagrams for one- (a), two- (b), and three-mirror (c) telescope designs with the mirror and FPA locations annotated.

Figure 2. Ray Trace Diagrams for a One- (a), Two- (b), and Three-Mirror Telescope (c). Adapted from [6].

Besides the number of mirrors, the shape of the mirror also plays a role in correcting optical aberrations. The shape can be parabolic, ellipsoidal, or hyperbolic. Similarly to that of the number of mirrors, the shape of the mirror has the capability to correct for some aberrations. For example, consider a two-mirror system in which the primary is a paraboloid, the second conic surface will be located so that its foci is coincident with that of the primary mirror. The secondary mirror can either be an ellipsoid or a hyperboloid. When the secondary mirror is an ellipsoid, it is called a Gregorian telescope; when it is a hyperboloid, the term Cassegrain telescope is used. The differences in these designs is shown in Figure 3. A three-mirror system would look similar.



Bely [10] showed how two-mirror conic Gregorian (a) and Cassegrain (b) telescope designs differ in relation to the shape of the secondary mirror. Both secondary mirrors are able to correct for spherical aberrations and are dominated by coma, but the Gregorian has a smaller image surface curve while the Cassegrain has a more compact telescope tube length.

Figure 3. Two-Mirror Conic Surface Design Options. Source: [10].

The general formula for expressing the conic surface of a mirror is given by

$$\rho^2 - 2Rz + (1 - e^2)z^2 = 0, \quad (2.1)$$

where the eccentricity of the conic is e , R is the radius, ρ is the running surface radius, and z is the size.

A multi-mirror telescope can be compared to that of a single mirror system through what is known as the equivalent focal length, $f\#$. This is often expressed in terms of a ratio, and is also known as the focal ratio, the f number, or N ,

$$f\# = N = \frac{f}{D}, \quad (2.2)$$

where f is the focal length and D is diameter of the mirror. These values are important in mirror fabrication as they relate directly to the required curvature of the mirror. In general, the larger the $f\#$, the easier the mirror is to fabricate. This especially holds true for large mirrors in which structural supports must be considered. Ideally, the mirror should be self-supporting to reduce weight, cost, materials, and complexity. However, the FOV and the $f\#$ are inversely proportional. Additionally, the larger the $f\#$, the larger the given cut-off frequency will be. These larger values necessitate an overall more complex optical system.

Many of the factors related to the telescope design have competing requirements. A value called “Optical Q” is the ratio of the resolution of the optics to that of the pixel size on the FPA and can be expressed as

$$Q = \frac{\lambda f \#}{p}, \quad (2.3)$$

where the value p represents the size of the pixel on the focal plane array and λ is median wavelength of interest. Optical Q provides the maximum resolution that can be afforded by diffraction with the minimum number of pixels. A large value of Q reduces the ground sampling distance, but too large of a value increases exposure time, making the system more susceptible to the effects of jitter. Too small of a Q reduces resolution and can cause the system to cut off before the Nyquist limit. A value of one has traditionally been used for remote sensing satellites, as seen in Figure 4.

| | French Satellites | | | US Satellites | | | | |
|--|-------------------|--------|----------|---------------|-------------|-------------|----------|-------------|
| | SPOT 1- 4 | SPOT 5 | Pleiades | Ikonos II | QuickBird 2 | WorldView 1 | GeoEye 1 | WorldView 2 |
| Mean Wavelength, λ_{mean} (μm) | 0.615 | 0.615 | 0.655 | 0.675 | 0.675 | 0.675 | 0.675 | 0.675 |
| Aperture diameter, D (m) | 0.31 | 0.31 | 0.65 | 0.70 | 0.6 | 0.6 | 1.1 | 1.1 |
| λ_{mean}/D , (μr) | 1.98 | 1.98 | 1.01 | 0.96 | 1.13 | 1.13 | 0.61 | 0.61 |
| Pixel pitch, p (μm) | 13 | 4.6 | 9.12 | 12 | 12 | 8 | 8 | 8 |
| Focal length, f (m) | 1.08 | 1.08 | 12.905 | 10 | 8.84 | 8.00 | 13.3 | 13.3 |
| IFOV, (μr) | 12.0 | 4.3 | 0.7 | 1.2 | 1.4 | 1.0 | 0.6 | 0.6 |
| F# | 3.48 | 3.48 | 19.85 | 14.29 | 14.73 | 13.33 | 12.09 | 12.09 |
| Optical Q | 0.165 | 0.466 | 1.426 | 0.804 | 0.829 | 1.13 | 1.02 | 1.02 |
| Eff. angular res., α_{eff} (mr) | 12.8 | 5.3 | 1.4 | 1.8 | 2.1 | 1.8 | 1.0 | 1.0 |
| Altitude, h (km) | 828 | 828 | 693 | 682 | 451 | 497 | 685 | 773 |
| Resolution, $\Delta = r \cdot \text{IFOV}$ (m) | 10.0 | 3.5 | 0.49 | 0.82 | 0.61 | 0.50 | 0.41 | 0.46 |
| Eff. ground res., Δ_T (m) | 10.6 | 4.4 | 1.00 | 1.24 | 0.94 | 0.88 | 0.70 | 0.78 |

Auelmann [11] tabulated a variety of key performance values for several factors related to the design of a telescope for several of the most well-known remote sensing optical satellites.

Figure 4. Key Properties for a Selection of Optical Remote Sensing Satellites.
Source: [11].

E. ENVIRONMENTAL CONSIDERATIONS

The mirror must maintain a fairly constant temperature across its surface in order to avoid thermal gradients. These gradients would otherwise distort the curvature of the mirror and adversely affect the optical path. This requirement presents a challenge as the

vehicle goes in and out of Earth's eclipse at a periodicity as low as 90 minutes. A CFRP mirror has a low thermal expansion coefficient and a low thermal conductivity value. These parameters prevent the mirror from deforming appreciably with temperature changes. However, when it does experience a change, the mirror quickly adjusts to the temperature of its surroundings. The thermal properties and low-density material of CFRP make it a prime candidate as an alternative material for the primary mirror.

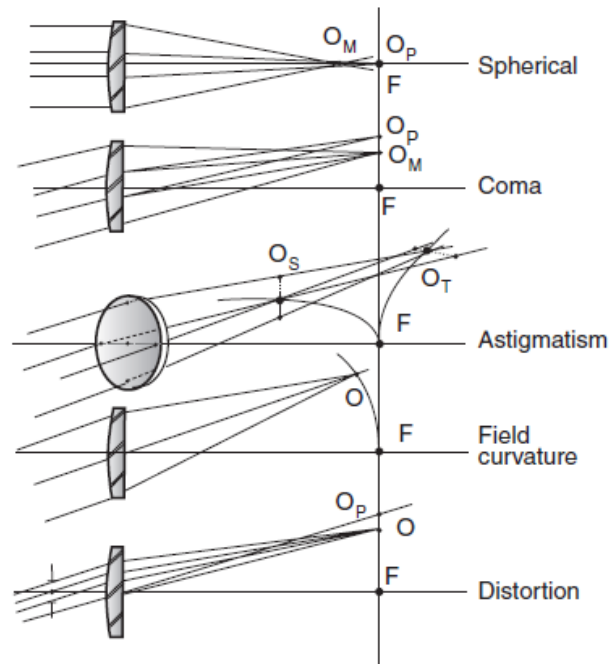
Contamination of the mirror is another area of concern. Particles can adhere to the mirror surface as a result of the manufacturing process, from outgassing in space, or from natural particulates found in orbit. Ionized particles from the space vehicle's propulsion system can also adhere to the mirror's surface. The contamination does not cling evenly to the surface, which causes localized areas of uncleanness. Besides disrupting the wavefront at the concentrated area, fogging of the mirror surface can occur. Contamination will also decrease the reflectivity of the mirror, which results in localized heating. The heating is a consequence of the absorptivity and emissivity at the contamination site no longer being equal to that of the rest of the mirror. This temperature difference can cause mirror distortion, which adversely affects the wavefront.

Lightweight materials help reduce launch costs by reducing mass. However, the space vehicle must be able to withstand the high stresses experienced during liftoff in addition to those of the space environment. The more rigid a structure is, the greater its ability to withstand the launch environment. However, the rigidity of the material also negatively affects the ability of the system to correct for low-order optical errors once on orbit.

Preventing stray light from other light sources and thermal emission are additional considerations. Baffles help control the amount of unwanted light from reaching the sensor. These devices also aid in preventing contamination of optical surfaces in the telescope. Contamination will decrease the amount of photons reaching the sensor due to the decreased reflectivity in addition to thermal effects.

F. OPTICAL SOURCES OF ERROR

Aberrations can result from errors in the optical path due to the design as well as errors induced by thermal effects or gravity. Challenges arise as the system is designed, built, and tested in a one-g (Earth surface) environment, but will operate at zero gravity. The five primary aberrations are shown in Figure 5.



Bely [10] shows the five primary optical aberrations affecting telescopes. The first one, spherical, is a result of light rays not converging at the same location and is the only aberration with effects on axis image quality. The remaining aberrations are dominant when looking off axis. Coma is a result of off axis light rays not converging at the same location. Astigmatism comes from a difference in focus between light in the perpendicular direction and that of the on and off axis plane. Field curvature happens when the image forms on a curved surface instead of a plane. Distortion is a consequence of scaling due to differences in path length caused by field angles.

Figure 5. The Five Primary Optical Aberrations. Source: [10].

The last four aberrations in Figure 5 are the result of off-axis light. Off-axis light is a function of geometry, which is dependent on the path of the incoming light. These distortions are known as high-order aberrations. Multi-mirror systems are preferred as

they can correct for these higher order aberrations with the addition of each additional tertiary mirror.

Diffraction occurs when light hits the edge of an object and bends around it. This causes the light to spread [12]. Dust and particulates in space and in the atmosphere can cause light to diffract. Diffraction will cause images of a point source to appear blurred and with haloes. It is important that surfaces inside a telescope are as smooth as possible in order minimize the amount of diffraction from reflection. Imperfections in the design can also cause further diffraction of the light and distortion of the wavefront. This case will be seen later in Chapter V in the design of the simulated telescope.

G. WAVEFRONT ERROR

Collectively, all sources of error can be combined into what is known as the wavefront error. The primary mirror is considered to be the reference surface. The difference between the wavefront at the reference surface and that of the wavefront at the sensor is called the wavefront error. The magnitude of the error is the root mean square (RMS). The RMS can be quantified in terms of nanometers or as fraction of the wavelength and is calculated by

$$RMS = \sqrt{\frac{\sum_{i=1}^N \phi_i^2}{N}}, \quad (2.4)$$

where ϕ is the wavefront measured, while N is total number of wavefronts recorded. For this report, RMS will be considered in terms of wavelength. “Near-perfect” conditions result when the RMS error is less than the wavelength divided by fourteen [10].

H. FIELD ANGLE MAGNIFICATION

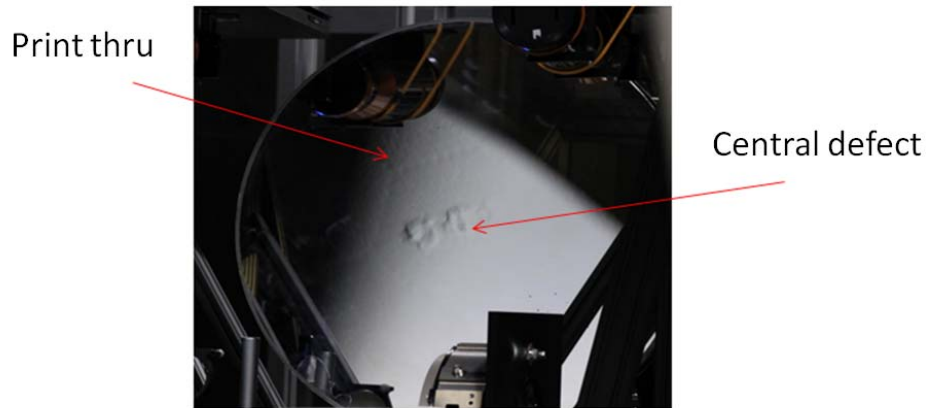
Field angle affects are a result of the linear approach due to the paraxial optics method. This approach relates the angles and heights of a ray traversing through a system. It assumes that a plane wave reaches a point all at once for a given time. However, this assumption does not hold true due to differences in the path length of the light for a wide field of view system. In such a telescope, the FOV is steered across the FOR resulting in light reaching the detector at different times. This is of particular

importance because the optics in a telescope have a magnifying effect that results from the difference in diameter of the primary mirror and that of the DM. Magnification dramatically increases the small differences seen at the primary mirror when compared to the DM. This means that the edges of the FOV are more prone to error than the center. If the magnification is too high, a deformable mirror will not be able to correct for the full FOV. Too great of a magnification will saturate the DM's actuator stroke, preventing further correction of the wavefront. The effects of magnification and how it relates to the required actuator stroke of a DM will be seen in Chapter IV.

III. EXPERIMENTAL SETUP

A. CFRP CORRECTION

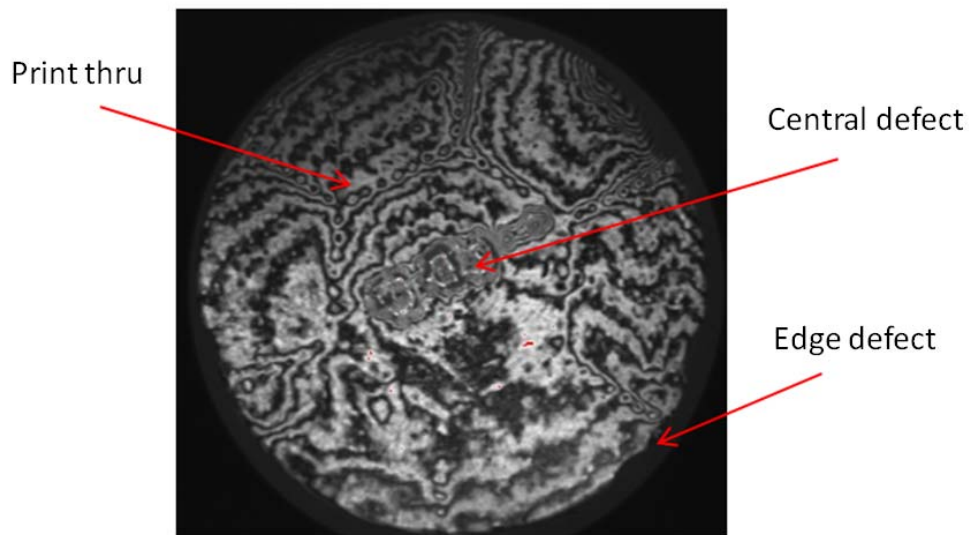
A one-meter cell-type core structure CFRP mirror was supplied to NPS in 2015. The mirror has an aluminum face sheet optimized for the visible spectrum and is shown in Figure 6.



A one-meter parabolic aperture carbon fiber reinforced polymer (CFRP) mirror with cell type core structure manufactured by Composite Mirror Applications. The mirror was developed in collaboration with the Naval Research Laboratory (NRL) and Sandia National Laboratories to support the development and manufacturing of large thin-shelled mirrors. The mirror is a manufacturing demonstrator that suffers from numerous fabrication defects.

Figure 6. One-Meter NPS CRP Mirror

The mirror suffers from several defects that occurred during the manufacturing process. These errors include print thru of the core to the mirror surface and surface defects at the center of the mirror as well as edge defects. These errors occurred when the mirror was removed from the mandrel [13]. All defects are clearly visible in the interferometric reading shown in Figure 7.

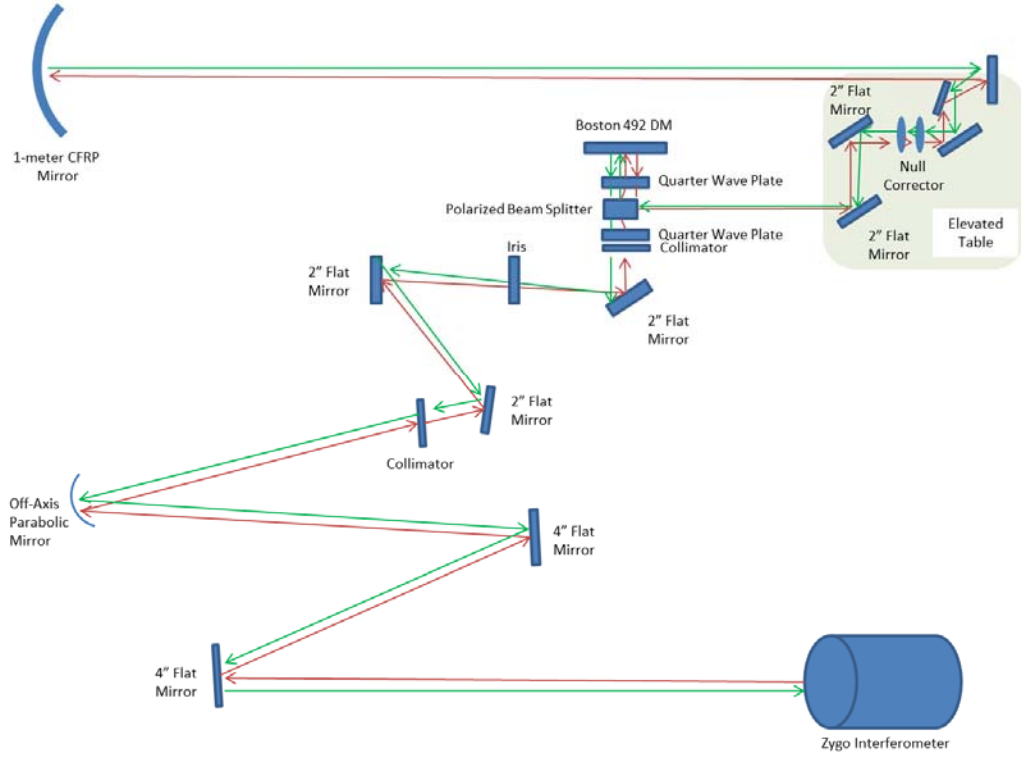


This image is an interferometric measurement of the CFRP mirror before being reflected off of the DM. All optical defects are easily visible as annotated. The large number of fringes on the surface indicates that the mirror is of very poor optical quality.

Figure 7. NPS CFRP One-Meter Mirror Interferometric Measurement

The poor optical quality of the CFRP mirror can be seen in the optical fringes that appear in Figure 7. The fringes are denoted by the black and white stripes seen throughout the image. Each subsequent set of fringes is a difference of one wavelength in phasing. The number of fringes in an interferometric reading is an indication of how focused the image is. The number of fringes should be kept to a minimum. The large number of fringes present in the reading indicates the poor optical quality of the mirror.

The optical layout shown in Figure 8 has light starting at the interferometer and reflecting across a series of mirrors before reaching a Boston-492 DM. The quarter wave plates polarize the light so that as it reflects off the DM, the light is then redirected at the beam splitter to the one-meter CFRP mirror before returning back to the Zygo interferometer. The multiple combinations of two- and four-inch mirrors were necessary so that the system would have the correct focal length with the DM at the exit pupil.

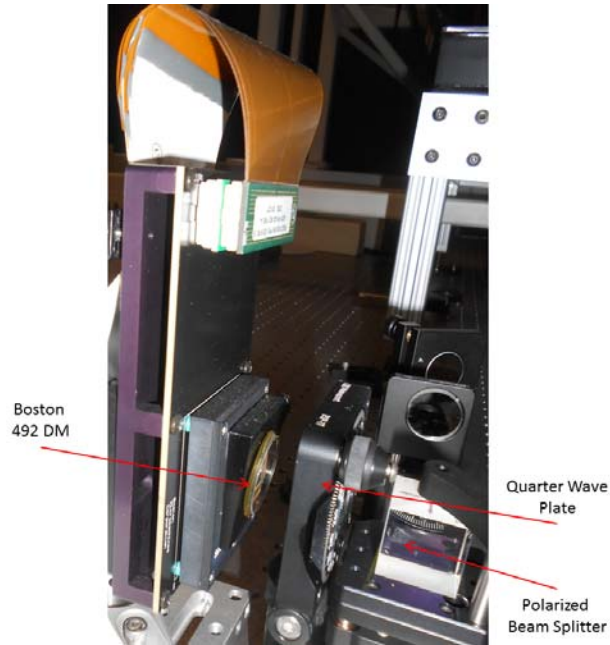


One-meter CFRP optical layout with the Boston 492 DM at the exit pupil location of the CFRP mirror. The red line indicates the beam's path from the interferometer to the CFRP mirror while the green line is the return path from the mirror to the interferometer.

Figure 8. Experimental Optical Schematic for the CFRP Mirror Correction

B. DEFORMABLE MIRROR

A segmented Boston Micromachines 492-SLM deformable mirror consisting of 492 actuators in a square pattern was used to correct the wavefront of the CFRP mirror. The device provides high-resolution control at a 60kHz frame rate. An image of the Boston 492 DM is shown in Figure 9 as it appears in the optical schematic from Figure 8.

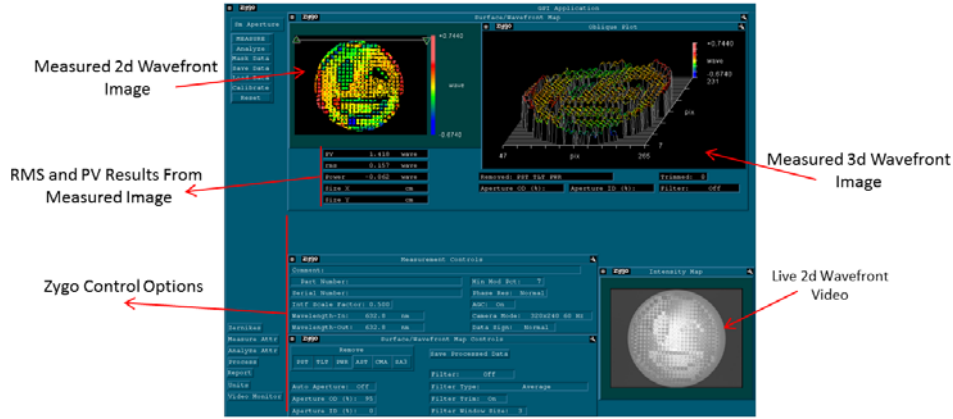


The DM is the small circular mirror annotated in the figure. The DM is encapsulated inside an enclosure that is wired bonded to chip attached to the circuit board behind the DM. The ribbon cable at the top of the image sends the appropriate voltage to each segment of the mirror. The Boston DM used in this experiment had three segments that were previously determined to be inoperable: 1, 43, and 61. At these actuator positions, the difference in wavefront position was set to zero so that the system would not attempt to correct these areas.

Figure 9. Boston 492-DM as Shown in the Optical Schematic from Figure 8

C. WAVEFRONT SENSING

A Zygo GPI XPHR laser interferometer operating at a wavelength of 632.8nm was used to sense the wavefront reflecting off the CFRP mirror. After the interferometer took a reading, the data was sent to MetroPro software for analysis. A screenshot from the MetroPro software with a measurement from the Boston DM is shown in Figure 10.

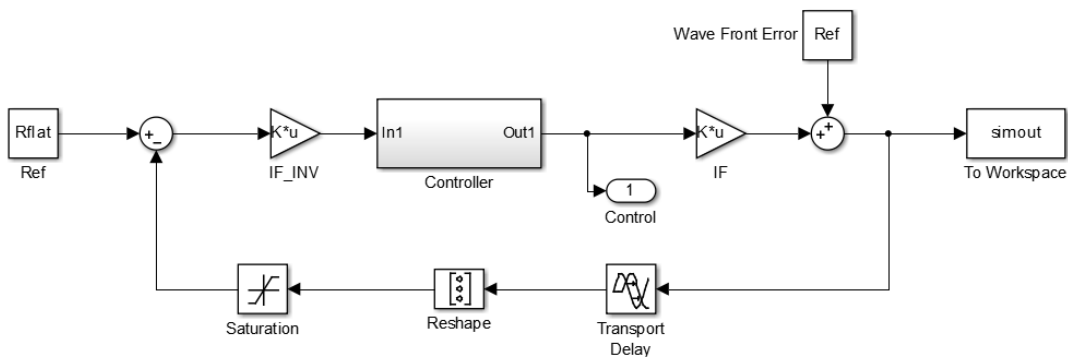


Screenshot from the MetroPro software displaying a reading from the Boston 492-SLM DM.

Figure 10. Screenshot from the MetroPro Software

D. CONTROL

The Boston DM can be commanded to apply various voltages to different actuator segments in order to vary the height of each segment as needed. An integral gain control law was established to compare the height of each actuator to that of a desired height. The control law attempted to minimize the height difference in each actuator compared to that of the desired state. This method constantly integrates the system error and attempts to correct the difference through a proportional integral law as shown in the Simulink file in Figure 11.



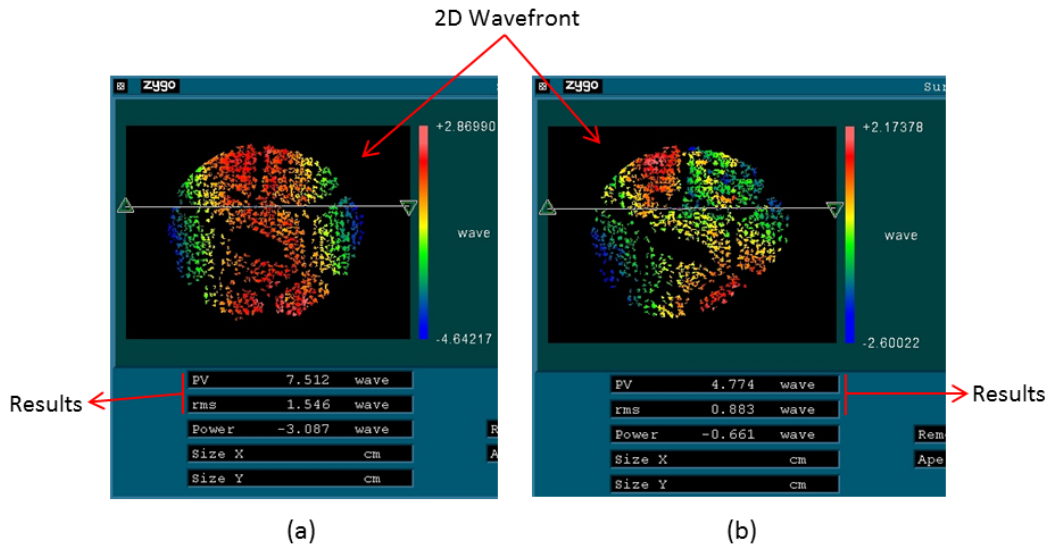
MATLAB Simulink integral gain control model. The desired shape of the mirror is input as Rflat while the actually measured data is the wavefront error. The system attempts to minimize the difference between these two values, taking into account saturation and a time delay.

Figure 11. Simulink Integral Gain Controller.

The voltage required to achieve the desired state in the control law was determined through

$$u(k+1) = u(k) + \alpha \phi_e(k), \quad (3.1)$$

where α is the update gain value while ϕ is the phase of the wavefront. The DM was commanded to correct for the surface errors of the CFRP mirror in order to minimize the wavefront RMS value. The before and after images as displayed by the MetroPro Software are shown in Figure 12.



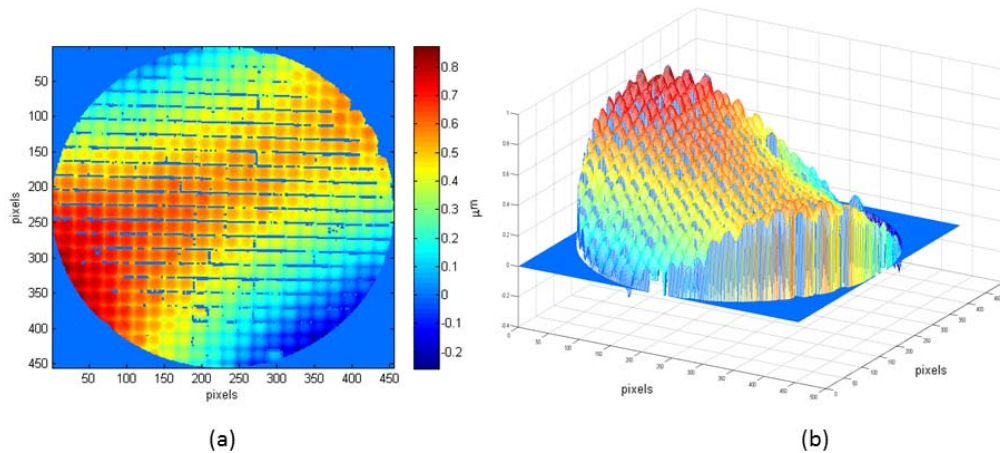
MetroPro screenshots of the CFRP mirror before (a) and after (b) correction by the Boston 492-DM. Areas in red indicate high points while blue areas indicate low points. Measurements were taken in relation to waves. For this experiment, a wavelength of 632.8nm was used. The before and after RMS values are located below the wavefront as annotated.

Figure 12. Before (a) and After (b) CFRP Mirror Correction by the Boston 492-DM

Before correction, the CFRP mirror had a peak to valley of 7.512 waves and a RMS value of 1.546 waves. After correction by the DM, the CRP mirror had a peak to valley of 4.774 waves and an RMS value of 0.883 waves. While the corrected wavefront is still not perfectly flat, the DM was able to reduce the wavefront error by approximately half the original value, despite the extremely poor initial optical quality of the mirror.

Utilizing a mirror with improved optical quality could result in further progress in decreasing the RMS value. Additionally, using a different DM with another surface type (such as a continuous DM), or a DM with a greater number of actuators or a DM with greater stroke, all additionally have the potential to further improve the RMS value.

Ideally, Figure 12 should appear as a monochromatic circle without any black dots or lines appearing inside the disk. However, black spots are clearly present in the figure. These spots represent dropouts in the data due to the interferometer being unable to take a measurement. Dropouts due to the mirror fabrication process are seen as large black spots while the smaller black regions in a checkerboard pattern are a result of the gaps between actuator segments. Mueller [14] previously characterized the dropout due to the gaps between segments for the DM by taking an interferometric reading of the DM surface. His results appear in Figure 13.



Mueller [14] measured the 2D (a) and 3D (b) surface map for a segmented DM. The gap between segments of the DM is clearly visible as the vertical and horizontal lines seen in (a) and (b). These lines indicate pixel locations where the interferometer was unable to take a measurement.

Figure 13. 2D (a) and 3D (b) Wavefront of Segmented Boston 492 DM.
Source: [14].

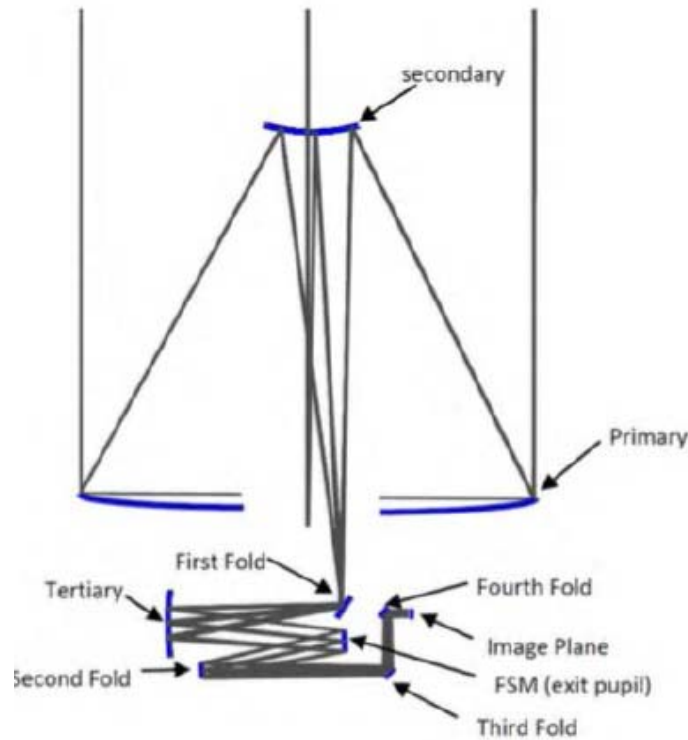
The checkerboard pattern in Figure 13 correlates well to the pattern seen in Figure 12, suggesting that the DM is the source.

THIS PAGE INTENTIONALLY LEFT BLANK

IV. NOTIONAL TELESCOPE DESIGN AND CORRECTION

A. TELESCOPE DESIGN

A notional optical telescope was designed using NPS' SMT as a starting point to evaluate figures of merit for a DM placed at the exit pupil. Because the SMT has an extremely complicated telescope design, several modifications were made in order decrease the scope. The three-mirror hyperbolic optical layout for the SMT is shown in Figure 14.

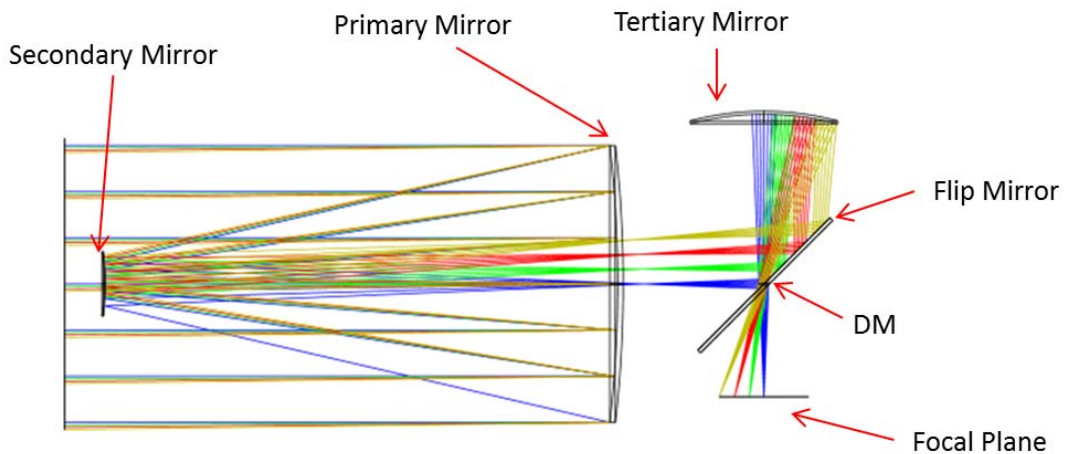


Allen [9] sketched the optical layout of the SMT. The design was the starting part in building a simpler model to test the previously constructed DM models. The blue surfaces indicate the position of various mirrors in the system while the gray lines represent the light rays reflecting off the various surfaces.

Figure 14. Optical Layout of the SMT. Source: [9].

The first fold of Figure 14 brings the light rays off axis in order to avoid blocking the beam, while the tertiary mirror creates a real exit pupil at the fast steering mirror

(FSM). The ideal location for the DM is at the exit pupil: in the SMT design, the FST is located at the exit pupil. To place a DM at this point would require the FSM to also be a DM. Such a design would not only increase complexity but would require the size of the DM to match the diameter of the exit pupil. At the current location of the FSM the exit pupil has a diameter of 150mm. A gimballed FSM of this size is not commercially available. Therefore, the FSM was removed from the telescope design and replaced with a DM. The simplified design will be limited to looking on axis and will have small field angle magnification effects. Additionally, instead of using a segmented primary mirror, a passive three-meter monolithic mirror was used in order to more closely resemble the remote sensing satellites currently in orbit. Figure 15 shows the ray trace diagram of the Zmax model for the simplified design. The model was designed for simulations only and is not meant to represent an engineering model. The four colors in the diagram, blue, green, red, and yellow represent field angles of 0.0, 0.25, 0.5, and 0.75 degrees, respectively. The location of the DM is at the exit pupil, which is where the four colored rays converge, as annotated in Figure 15.



This ray trace diagram developed in Zmax for a three-meter hyperbolic telescope features multiple field angle aberrations. Blue rays indicate the path of light for on-axis viewing. Green rays are 0.25 degrees, red 0.5 degrees, and yellow 0.75 degrees off axis, respectively.

Figure 15. Zmax Ray Trace Diagram for Notional Telescope

Two simulations were conducted utilizing the telescope developed in Figure 15. In the first simulation, all mirrors in the telescope had perfect surfaces with no defects. The only wavefront aberrations in this system were a result of field angle magnification effects, or as result of errors inherent to the design of the telescope. Utilizing a previously developed DM model built by Mueller [14], a 100-actuator continuous DM in a 10 x 10 rectangular configuration was placed into the control law developed in Chapter III.

In the continuous DM model, Mueller [14] developed the influence function for the DM as a cubic form. The influence function is the shape of the mirror surface in response to a single actuator being actuated. Each actuator has its own influence function; these can collectively be combined into columns to form the influence matrix. This matrix is the collective response of the mirror surface in response to multiple actuators being actuated. The following Gaussian influence function was used to generate the displacement for the mirror's surface

$$W(x, y) = \frac{2\pi}{\lambda} \exp \left\{ \frac{\ln b \left[(x - x_c)^2 + (y - y_c)^2 \right]}{d^2} \right\}, \quad (4.1)$$

where d is the spacing between actuators and b is the Gaussian index [15]. The desired mirror shape is $W(x, y)$. The desired shape is then associated with a voltage, V_c , which controls the height of each actuator in relation to a specific actuator number c for the coordinate plane. The total number of actuators is R . The desired mirror shape can be expressed in the following relationship.

$$w(x, y) = \sum_{c=1}^R V_c W_c(x, y) \quad (4.2)$$

The model developed using this method was previously validated by comparing a surface map measurement taken by Bifano et al. [16] and associating the model results with actual measurements. The results of this comparison are shown in Figure 16.

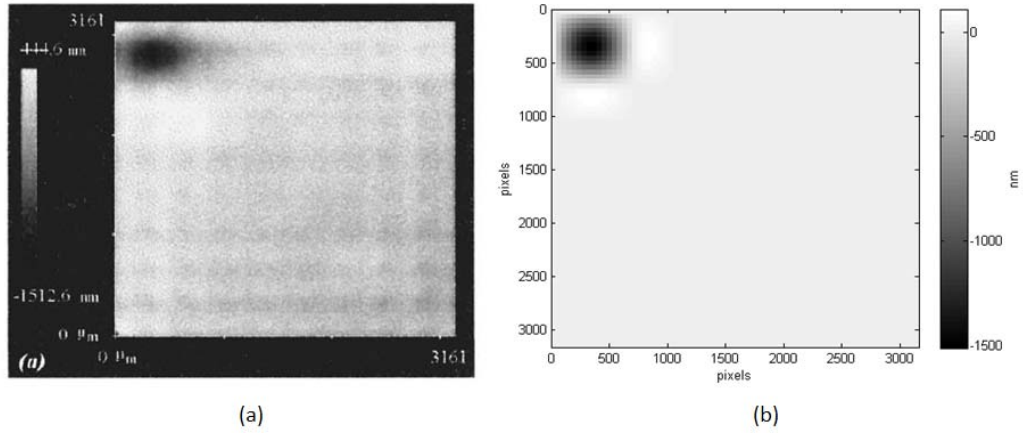
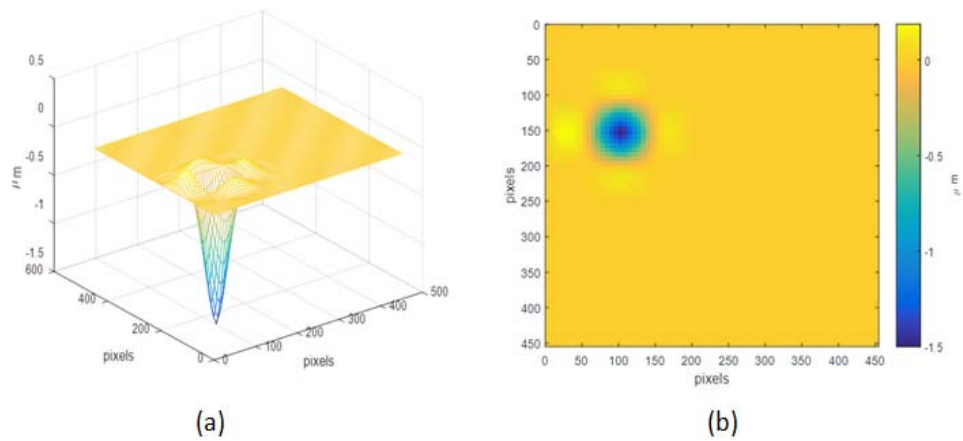


Figure 16. Experimental (a) and Model Results (b) of a Continuous DM.
Source: [14].

As seen in Figure 16, the results of the model are in agreement with the measured data. A single actuator influencing its neighbors is present in both images in addition to the correct pull down depth for the actuator when a voltage is applied. The results from Figure 16 were reconstructed in Figure 17 by having a voltage sent to actuator 24 so that the surface would be pulled down.



Actuator 24 can be seen altering the surface of its neighbors when actuated. Blue indicates a lower region while lighter colors indicate a higher one. On either side of actuator 24 the surface edges of its neighbors lift up slightly.

Figure 17. 3D (a) and 2D (b) Surface Plots of Actuator 24

The 2D images in Figure 16 and 17 agree with one another, indicating that the model was correctly translated from the previous work. The effect actuator 24 has on its neighbors is important as it correctly indicates the coupled nature of the system. When correcting for a wavefront, the DM must not only make adjustments for the surface error, but also for the deformation of neighboring actuators that cause undesired effects.

B. FIELD ANGLE CONSIDERATIONS

In order to study field angle effects, the optical path difference between rays needed to be resolved. McComas et al. [17] proposed a method to solve for the field angle effects by accounting for the difference in angles as seen at the primary and deformable mirror. To do this, he made the following four assumptions: 1) a perfect wavefront was entering the telescope; 2) the primary mirror had distortions; 3) the DM and primary mirror surfaces were conjugates; and 4) the DM and primary mirror were not the same size. Based upon these assumptions, he derived Equation 4.3,

$$\omega_R = \frac{4\pi}{\lambda} d_{PM}(x, y) \cos(\theta_{PM}) - \frac{4\pi}{\lambda} d_{DM}(x, y) \cos(\theta_{DM}), \quad (4.3)$$

where ω_R is the wavefront error to be corrected and d_{PM} and d_{DM} are the surface of the primary and deformable mirrors. The value θ represents the field angle as seen by both mirrors. McComas et al. were able to relate the difference in field angles seen by the mirrors by relating this angle to a magnification factor M in the following relation

$$\theta_{DM} = M \theta_{PM}. \quad (4.4)$$

The telescope created in Figure 15 for the first two simulations had a magnification factor of 30 based upon the size of the primary mirror in relation to the width of the rays at the exit pupil. The magnification relationship allows for Equation 4.1 to be written as

$$\omega_R = \frac{4\pi}{\lambda} d_{PM}(x, y) \cos(\theta_{PM}) - \frac{4\pi}{\lambda} d_{DM}(x, y) \cos(M \theta_{PM}). \quad (4.5)$$

From Equation 4.5 it can be seen that as the angle increases, so too does the path error, which makes the resulting error more difficult to correct. The magnification effect was accounted for in the development of the Zmax telescope model. In addition to

increasing certain portions of the wavefront, field angles cause the image to move in relation to the FPA.

From the Before RMS value in Table 1 it can be seen that with each additional quarter degree off nadir, the RMS value before correction more than doubled. This is significant because the corrected RMS values after did not keep pace with the Before RMS values. However, through correction some reduction in the wavefront was achieved for all angles.

Table 1. Table of Results for Field Angle Only Correction

| | 0.0 (deg) | 0.25 (deg) | 0.5 (deg) | 0.75 (deg) |
|------------|-----------|------------|-----------|------------|
| RMS Before | 0.0072 | 0.0688 | 0.1373 | 0.3217 |
| RMS After | 0.0016 | 0.0161 | 0.0348 | 0.0738 |

MATLAB RMS results for the notional telescope simulation with perfect mirrors. The system suffers only from field magnification effects. Correction was done by a notional 10x10 continuous DM with a stroke limit of $3\text{ }\mu\text{m}$. RMS value is denoted in waves.

The Before RMS value at zero degrees for the perfect mirror system should be zero according to Equation 4.5; however, this is not the case (as seen in Table 1). The nonzero result indicates that the simulated telescope design has some inherent aberrations present due to the optical design.

The second simulation incorporated the measured wavefront from the one-meter CFRP mirror from the experiment in Chapter II and translated that surface onto the three-meter mirror in Figure 15. However, before this could be done, the experimental data needed to be fitted to Zernike polynomials to account for the data points that could not be measured by the interferometer.

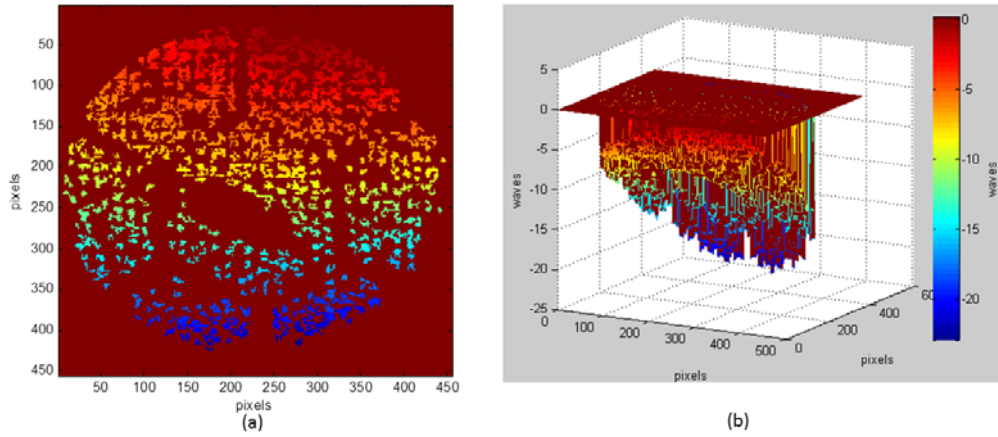
C. ZERNIKE POLYNOMIALS

Zernike polynomials are orthogonal to a unit disk that can extend to an infinite number. For this study, only third-order polynomials or less were considered. To create a wavefront, the polynomials can be summed by matrix inversion in order to fill in the missing data,

$$\varphi(\rho, \theta) = \sum_{i=1}^M a_i Z_i(\rho, \theta), \quad (4.6)$$

where $Z_i(\rho, \theta)$ are the fitted polynomials evaluated at (ρ, θ) on the unit disk. a_i represents the Zernike coefficients, while the number of Zernike fitted polynomials is expressed as M .

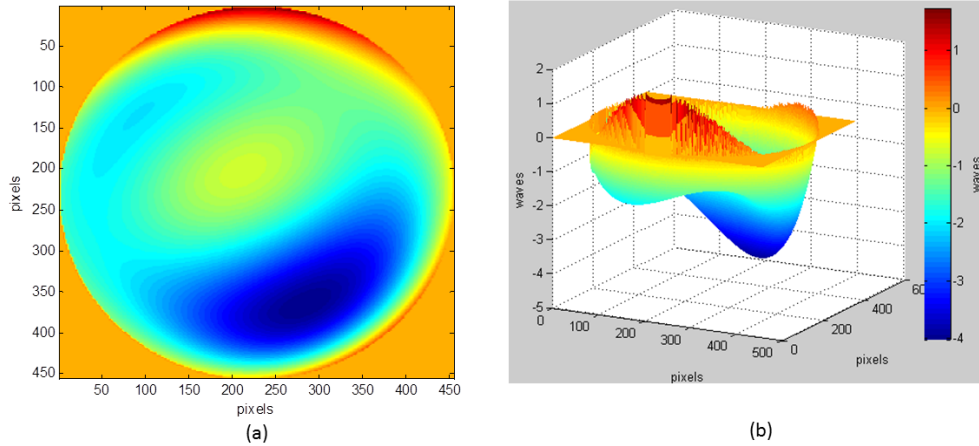
A raw image of the CFRP mirror before being fitted to Zernike polynomials is shown in Figure 18.



A 2D(a) and 3D(b) image of the CFRP mirror before correction is shown. The dark red indicates a portion of the data was dropped due to the interferometer being unable to take a measurement. The imperfections in the mirror due to fabrication are clearly seen in Figure 19 (a) as the dark red spot near the center in addition to the checkboard pattern created by the gaps between segments in the DM.

Figure 18. 2D (a) and 3D (b) Raw Wavefront Portion of CFRP Mirror

The data from Figure 18 was then fitted to third order and below Zernike polynomials in accordance with Equation 4.6, using a MATLAB script developed by the Naval Research Laboratory as part of research previously done at NPS. The results of the Zernike fitted data from Figure 18 for the CFRP mirror is shown in Figure 19.



2D (a) and 3D (b) images of a portion of the fitted CFRP mirror with the gaps in data filled in. Since the telescope has a circular primary mirror, the data was bounded as shown in (a) so it would fit the diameter of the notional telescope.

Figure 19. 2D (a) and 3D (b) Fitted Wavefront Portion of CFRP Mirror

The Zernike coefficients that created Figure 20 were then placed into the notional telescope shown in Figure 15 so that its primary mirror would have a similar wavefront to that of the CFRP mirror. The values of the coefficients for the mirror as calculated by the Zernike polynomial script are listed in Table 2.

Table 2. Table of CFRP Zernike Coefficients

| Zernike Order | Coefficient |
|---------------|-------------|
| 1 | -1.70 |
| 2 | -1.16 |
| 3 | 0.021 |
| 4 | 0.422 |
| 5 | -0.376 |
| 6 | -0.159 |
| 7 | 0.555 |
| 8 | 0.640 |
| 9 | 0.259 |
| 10 | -0.012 |
| 11 | 1.213 |
| 12 | 0.696 |
| 13 | -0.688 |

This is the list of Zernike polynomial coefficients generated for a portion of the CFRP mirror. These coefficients were generated in MATLAB and then transferred to the Zmax model shown in Figure 15 so that its primary mirror would have a similar wavefront.

The same four field angles were then applied to the second simulation. The results for the second simulation using a distorted mirror that utilized the coefficients from Table 2 are shown in Table 3.

Table 3. Table of Results for Field Angle and Primary Mirror Correction.

| | 0.0 (deg) | 0.25 (deg) | 0.5 (deg) | 0.75 (deg) |
|------------|-----------|------------|-----------|------------|
| RMS Before | 0.9865 | 1.0067 | 1.0613 | 1.1283 |
| RMS After | 0.3041 | 0.3147 | 0.3322 | 0.3124 |

Before and After correction MATLAB simulation RMS results for a telescope with a primary mirror that has a similar wavefront to that of the one-meter CFRP mirror at NPS. Correction was done by a simulated 10 x 10 continuous DM. The RMS values are denoted in waves using a wavelength of 632.8nm as was done in the experimental work.

The difference in RMS values between 0.0 and 0.75 degrees is approximately 0.14 waves for the distorted mirror simulation. In the perfect mirror simulation the difference was 0.31 waves. This disparity between simulations indicates that the distorted primary mirror surface in the second simulation is the dominant source of the wavefront error.

To evaluate how the number of actuators affects wavefront correction, a continuous DM with 361 actuators in a 19 x 19 configuration was constructed using the same model previously developed by Mueller [14]. This second model was then placed into the same two telescope simulations as was done with the 100 actuator model. For both the 100 and 361 actuator models, simulations using the two different primary mirror surfaces were run for strokes of 1, 3, and 5 μm , respectively. In total, 48 simulations were run using combinations of the previously mentioned variables in order to isolate how different parameters affect the RMS of the wavefront. The results from these simulations are summarized in Table 4.

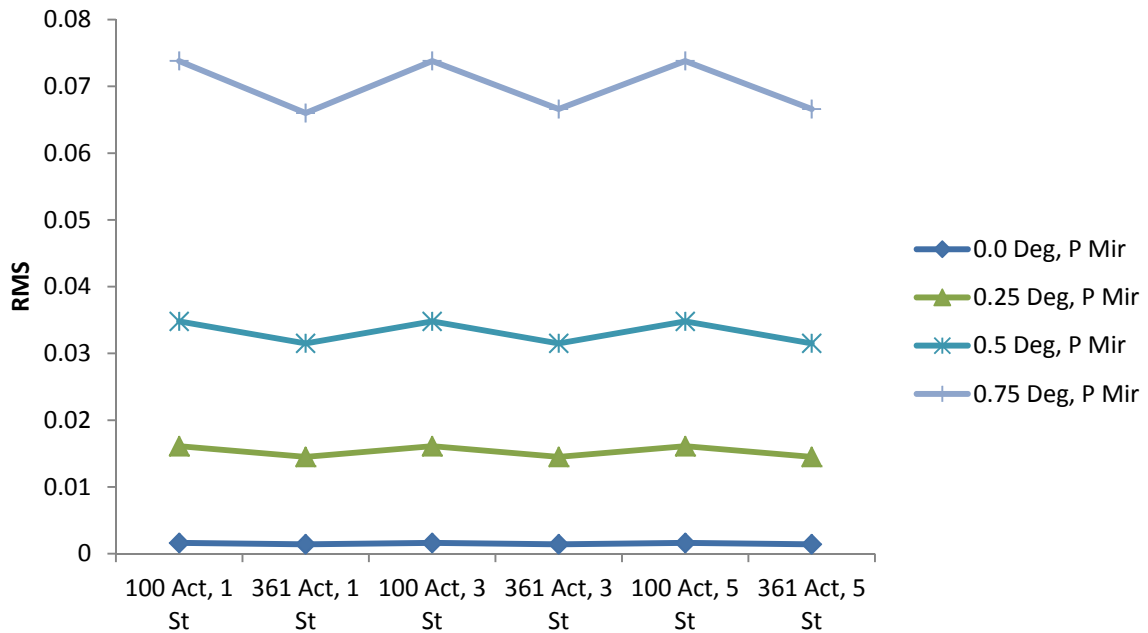
Table 4. Comparison of 100 versus 361 Actuator DM for Varying Strokes.

| Stroke (μm) | Actuators | 0.0 (deg) | | 0.25 (deg) | | 0.5 (deg) | | 0.75 (deg) | |
|-----------------------|-----------|--------------------|----------------------|--------------------|----------------------|--------------------|----------------------|--------------------|----------------------|
| | | Perfect Primary | Distorted Primary | Perfect Primary | Distorted Primary | Perfect Primary | Distorted Primary | Perfect Primary | Distorted Primary |
| 1 | 100 | 0.0016 | 0.3315 | 0.0161 | 0.3458 | 0.0348 | 0.3693 | 0.0738 | 0.3368 |
| | 361 | 0.0014 | 0.3046 | 0.0145 | 0.3186 | 0.0315 | 0.3416 | 0.066 | 0.3083 |
| 3 | 100 | 0.0016 | 0.3041 | 0.0161 | 0.3147 | 0.0348 | 0.3322 | 0.0738 | 0.3124 |
| | 361 | 0.0014 | 0.2738 | 0.0145 | 0.2834 | 0.0315 | 0.2992 | 0.0666 | 0.2812 |
| 5 | 100 | 0.0016 | 0.3041 | 0.0161 | 0.3146 | 0.0348 | 0.3320 | 0.0738 | 0.3124 |
| | 361 | 0.0014 | 0.2737 | 0.0145 | 0.2833 | 0.0315 | 0.2991 | 0.0666 | 0.2812 |

MATLAB RMS values in waves comparing notional continuous DMs of 100 and 361 actuators correcting perfect and distorted primary mirrors as a function of field angle magnification and DM actuator stroke length.

As seen in Table 4, despite increasing the actuator count by over two hundred percent when going from 100 to 361 actuators, the resulting change in the RMS value had a negligible effect on the perfect primary mirror for all field angles. The RMS decreased only slightly when the mirror's surface was distorted. This indicates a nonlinear relationship between the number of actuators and the resulting RMS values. The same diminishing return can be seen in the stroke of each actuator. When going from a stroke of 1 to 3 μm there was a significant decrease in RMS; however, from 3 to 5 μm the differences were nearly nonexistent with changes only at the tens of thousandths of a wave. Additionally, when the primary mirror was perfect, increasing the stroke did little to reduce the RMS value any further past a point for each field angle.

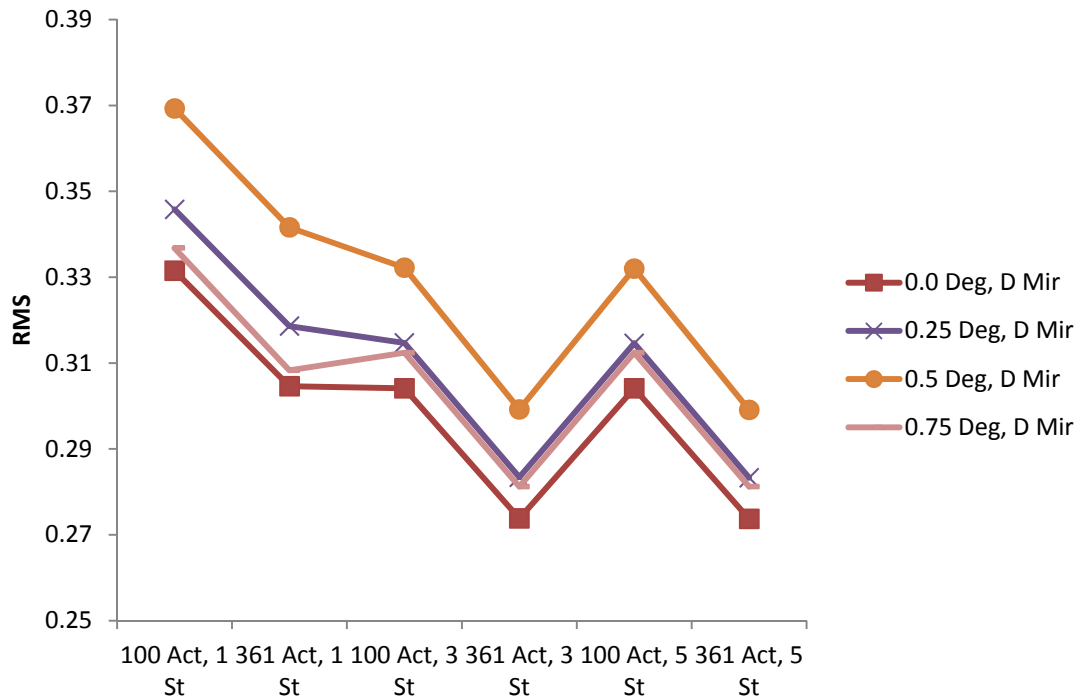
Table 4 data points were converted into a series of plots to better show trends in the data for each variable. The different field angles for both the 100 and 361 actuator simulations are compared in relation to actuator stroke length in Figure 20.



This chart compares the field angles in relation to the number of actuators and stroke of actuators compared to the resulting RMS for the perfect mirror simulation.

Figure 20. Perfect Primary Mirror Comparison of Variables

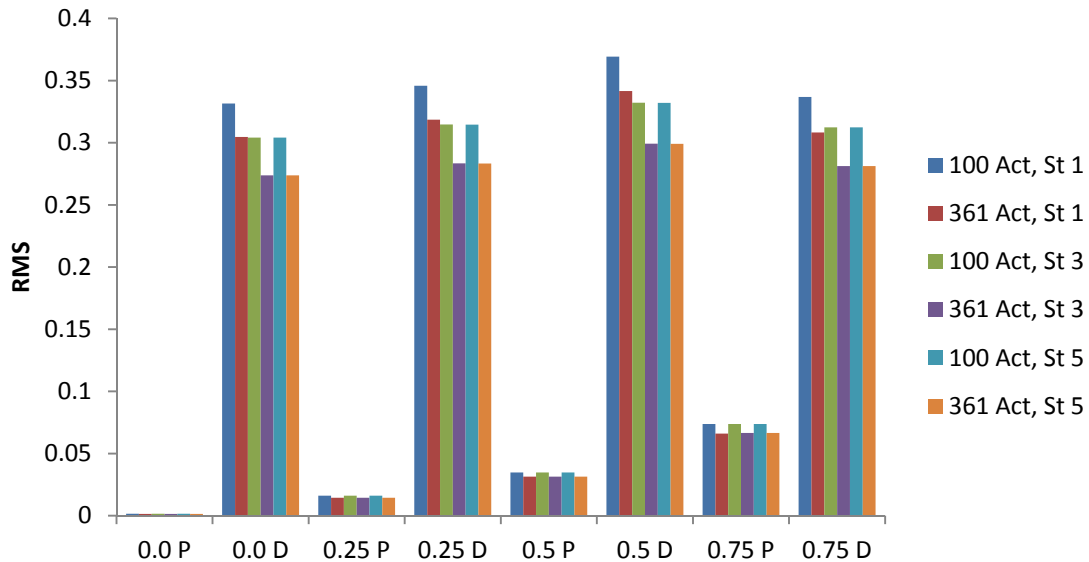
A slight improvement in the RMS values for all cases is seen when going from a 100 to a 361 actuator DM, as seen in Figure 20. However, further improvement was minimal in relation to stroke length. When reading Figure 20 from bottom to top, as the field angle increases, the number of actuators plays an increasingly significant role in decreasing the RMS value when going from 100 to 361. This can clearly be seen when comparing 0.0 degrees versus 0.75 degrees. At 0.0 the line appears nearly flat while at 0.75 degrees the line has a “W” appearance. This indicates that increasing the actuator count is best suited for situations involving large field angles. This relationship is due in part to the magnification factor. The same variables as compared in Figure 20 are again compared in Figure 21 for the distorted mirror scenario.



This chart compares the field angles in relation to the number of actuators and the stroke of each actuator compared to the resulting RMS value for the distorted mirror simulation.

Figure 21. Distorted Primary Mirror Comparison of Variables

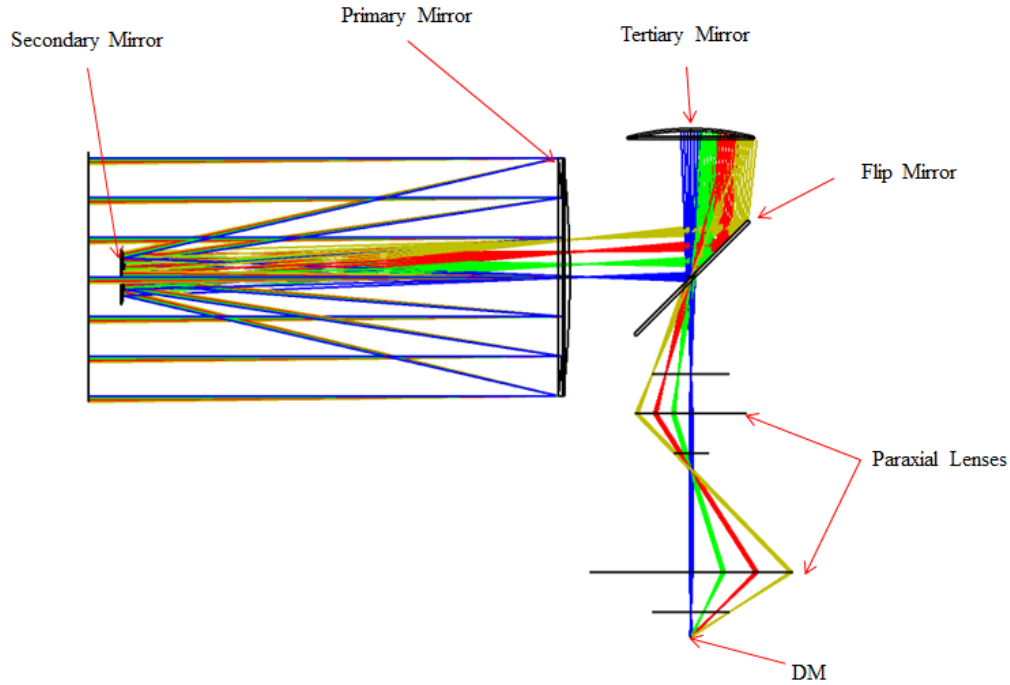
A greater decrease in RMS value for each actuator count in relation to an increase in stroke length of an actuator is shown in Figure 21. The graph shows that for a distorted mirror, a DM with both a higher actuator count and a larger stroke are the key parameters to improve when increase wavefront correction. However, the characteristic “W” shape that appeared in Figure 20 appears to start taking shape midway through the figure. It is interesting to note that, with one exception, the slopes of the lines are fairly consistent across all field angles for both the number of actuators and the stroke length. Figure 20 and 21 are summarized in Figure 22, which compares all simulations, variables, strokes, and mirror condition that were shown in Table 4.



This chart simultaneously compares mirror type, field angles, actuator count and stroke distance. It is derived from the results shown in Table 4.

Figure 22. Bar Chart Comparing Variables to RMS

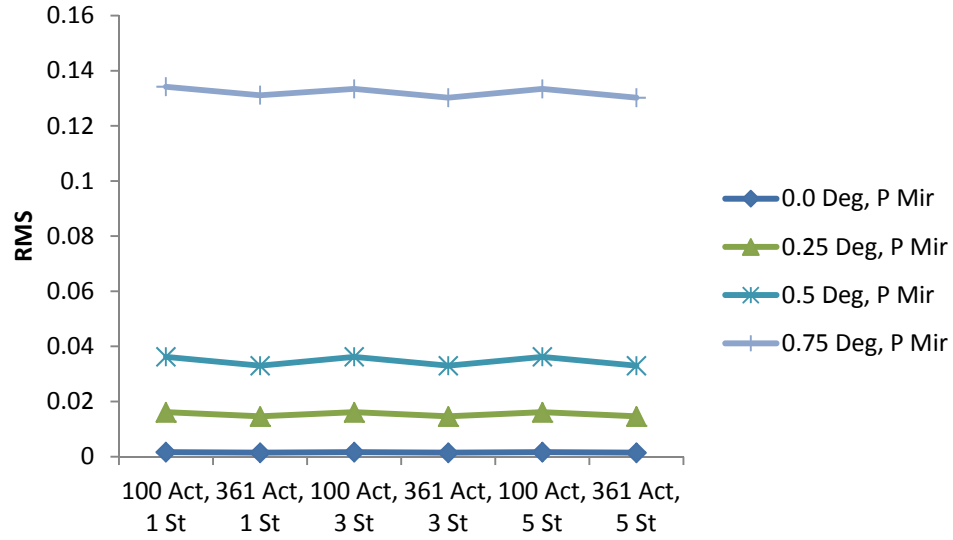
The model developed in Figure 15 had a magnification factor of 30. For the simulation to use a deformable mirror at a scale in which a microelectromechanical systems (MEMs) DM could be used would require the system to have a magnification factor of 100. The simulation was altered accordingly, as reflected in Figure 23.



This ray trace diagram developed in Zmax for a three-meter hyperbolic telescope features multiple field angle aberrations. Blue rays indicate the path of light for on-axis viewing. Green rays are 0.25 degrees, red 0.5 degrees, and yellow 0.75 degrees off axis, respectively. This system is similar to that of Figure 15 with the exception that it has a magnification factor of 100 in order to use a MEMs DM.

Figure 23. Zmax Ray Trace Diagram for Notional Telescope with a Magnification Factor of 100

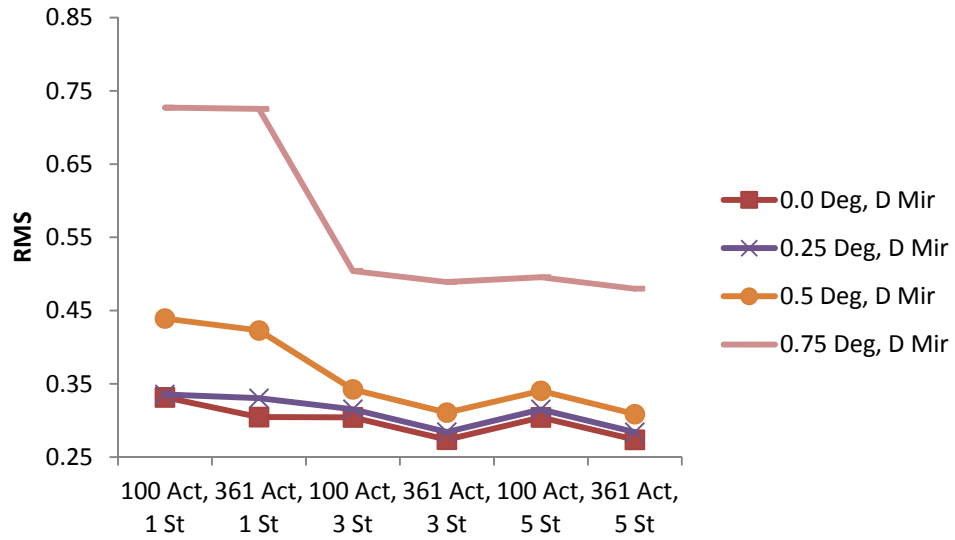
The same 48 simulations using the same variables were rerun, with the results depicted in Figure 24 and Figure 25.



This chart compares the field angles in relation to the number of actuators and stroke of actuators compared to the resulting RMS for the perfect mirror simulation at a magnification factor of 100.

Figure 24. Perfect Primary Mirror Comparison of Variables with a Magnification Factor of 100

Similar to Figure 20, Figure 24 displays the same characteristic shape with the exception of the RMS values at a field angle of 0.75 degrees. The error when going from 0.5 to 0.75 degrees is greatly magnified in the second scenario, suggesting a nonlinear relationship between field angles and magnification. Even with a perfect primary mirror using a stroke of $5\ \mu m$ the DM is unable to compensate for the wavefront error. Similarly, the distorted primary mirror scenario is shown in Figure 25.



This chart compares the field angles in relation to the number of actuators and the stroke of each actuator compared to the resulting RMS value for the distorted mirror simulation at a magnification factor of 100.

Figure 25. Distorted Primary Mirror Comparison of Variables with a Magnification Factor of 100

Figure 25 has the same trends seen in Figure 21 with the exception that the slopes of the lines for the various field angles are no longer the same. These results demonstrate that currently available MEMs DMs result in a substantial angular magnification factor that inhibits wavefront correction due to the larger field angles.

V. FUTURE WORK AND CONCLUSION

A. CONCLUSION

This thesis demonstrated how a DM could be used to reduce wavefront errors from surface imperfections on a mirror and to reduce field angle magnification effects. The simulated DM was able to correct the wavefront RMS value of a perfect primary mirror by ~125%, and the wavefront RMS value of a distorted primary mirror by ~100%. Wavefront error only slightly increased for higher order field angles. Potential DM limits were identified as being connected to the number of actuators on the DM and the stroke length of actuation. Both limits depended on the magnitude of the field angles and the magnification factor.

B. SUITABILITY OF MEMS IN THE SPACE ENVIRONMENT

DMs are designed to operate in a one-g environment. To be suitable for space-based applications, a device would need to function in zero gravity for sustained periods. The device must also withstand effects from the space environment including radiation and single event upsets. Further research could be done to characterize how a DM behaves differently in the two environments. Suggested studies include looking into the effects of operating in a vacuum, exposure to radiation, and error tolerance.

C. CONTINUOUS FACE SHEET MEMS DEVICE

In this research, a segmented mirror was used to correct a CFRP mirror. A continuous face-sheet mirror offers greater potential for error correction due to its smooth surface and ability to phase. Additionally, the gap between actuator segments that caused dropouts in data would not be present. A continuous DM would also increase the number of photons reaching the focal plane array, allowing for a decreased integration time. Experiments in the lab at NPS could be rerun using a continuous DM to compare performance of the two mirrors.

D. OFF AXIS TESTING

Further research could be performed on the effects related to field angle magnification. Experiments could be conducted in the laboratory using an actual DM for correction and to compare the experimental and simulation results. Additionally, a wide field of view telescope could be modeled such that it has larger field angles for which the DM must correct.

APPENDIX. CONTROL SCRIPT

```
clc;clear all; close all

K=input('What is the type of Device 1)Continous 2)Segmented 3)TipTilt
4)Sim Results no primary error 5) Sim with primary error 6)no primary
36lact 7)primary error 36lact ');
tic
if K==1;
    load continousIF
end
if K==2;
    load segmentedIF
end
if K==3;
    load tiptiltIF
end
if K==4
    load 100actuator
    A=input('What is the degree ');
    if A==0;
        load phi0
    end
    if A==0.25;
        load phi25
    end
    if A==0.5;
        load phi5
    end
    if A==0.75;
        load phi75
    end
end
end

if K==5
    load 100actuator

    A=input('What is the degree ');
    if A==0;
        load phiA0
    end
    if A==0.25;
        load phiA25
    end
    if A==0.5;
        load phiA5
    end
    if A==0.75;
        load phiA75
    end
end
end

if K==6
```

```

load 361actuator
A=input('What is the degree ');
if A==0;
load 361phi0
end
if A==0.25;
load 361phi25
end
if A==0.5;
load 361phi5
end
if A==0.75;
load 361phi75
end
end

if K==7
load 361actuator

A=input('What is the degree ');
if A==0;
load 361phiA0
end
if A==0.25;
load 361phiA25
end
if A==0.5;
load 361phiA5
end
if A==0.75;
load 361phiA75
end

end

if K==1 || K==2 || K==3
c=sqrt(length(IF));
[X,Y]=meshgrid(1:1:c);
W = sqrt(X.^2 + Y.^2);
Ref=0.25e-6*sin(0.1*W);
phi=0.25e-6*sin(0.1*W);
end

if K==4 || K==5 || K==6 || K==7
c=sqrt(length(IF));
%Ref=reshape(phi,113,113);
end

if K==1 || K==2 || K==3 || K==4
figure()
mesh(phi/1e-6);
h=colorbar
h=colorbar;
ylabel(h, 'waves')

```

```

        xlabel('pixels')
        ylabel('pixels')
        zlabel('waves')
    end

    Ref=reshape(phi',[numel(phi) 1]);

    R=size(IF,2); %Number of actuators

    Kp = 2;

    Rflat=zeros(length(Ref),1);

    IF_INV=pinv(IF);
    tf =2;
    [t,~,outputs] = sim('PINV_test',[0,tf]);

    simdata=simout.Data;

    figure()
    imagesc(reshape(simdata(:,:,1)/1e-6,[c,c]));
    colorbar
    figure()
    B=size(simdata);
    imagesc(reshape(simdata(:,:,B(length(B)))/1e-6,[c,c]));
    colorbar
    xlabel('waves')

    RMSbefore=rms(simdata(:,:,1))/632.8e-9
    PVbefore=(max(simdata(:,:,1))-min(simdata(:,:,1)))/632.8e-9

    RMSafter=rms(simdata(:,:,B(length(B))))/632.8e-9
    PVafter=(max(simdata(:,:,B(length(B))))-
    min(simdata(:,:,B(length(B)))/632.8e-9
    time=toc;

```

THIS PAGE INTENTIONALLY LEFT BLANK

LIST OF REFERENCES

- [1] U.S. Department of Defense, “National security space strategy.” Jan-2011
- [2] E. Hecht, *Optics*, 2nd Ed. Boston MA: Addison-Wesley Publishing Company, 1987.
- [3] B. K. McComas, “Configurable adaptive optics for the correction of space-based optical systems,” Ph. D. dissertation, Dept. of Electrical Engineering, University of Colorado, Boulder, CO, 2002.
- [4] R.N. Wilson et al., “Adaptive optics,” *Journal of Modern Optics*, vol. 38, no. 2, pp. 219–243, Feb. 1991.
- [5] E. Smith et al., “The next generation space telescope design reference mission,” *Proc. SPIE*, 1998, vol. 3356, 0277–786X.
- [6] L. Feinbert et al., “Space telescope design considerations,” in *Optical Engineering*, 2012, vol 51, 011006.
- [7] D. Baiocchi and H. P. Stahl, “Enabling future space telescopes: mirror technology review and development roadmap,” *Astro2010: The Astronomy and Astrophysics Decadal Survey*, 2009, vol. 2010, p. 23.
- [8] D. Baiocchi, “Design and control of lightweight, active space mirrors,” Doctoral dissertation, University of Arizona, 2004.
- [9] M. R. Allen, “Correction of a space telescope active optics in a woofer-tweeter configuration,” Ph. D. dissertation, Dept. of Mechanical and Aerospace Engineering Naval Postgraduate School, Monterey, CA, 2015.
- [10] P. Bely, *Design and Construction of Large Optical Telescopes*, New York NY: Springer-Verlag Publishing, 2003.
- [11] R. Auelmann. (2012, Nov). Image quality metrics. [Online]. Available <http://www.techarchive.org/wp-content/themes/boilerplate/largerdocs/Image%20Quality%20Metrics.pdf>
- [12] F. Pedrotti and L. Pedrotti, *Introduction to Optics*, 2nd Ed. Upper Saddle River NJ: Prentice Hall Publishing, 1993.
- [13] B. Agrawal et al., “Cost-effective aperture with deformable mirror for imaging satellites,” presented at the 66th International Astronautical Conference, Jerusalem, Israel, 2015.

- [14] M. Mueller, “Modeling of a micro-electronic-mechanical systems (MEMS) deformable mirror for simulation and characterization,” M.S. thesis, Space Sys. Dept., Naval Postgraduate School, Monterey, CA 2016.
- [15] H. Xing Yan et al., “Numerical simulation of an adaptive optics system with laser propagation in the atmosphere,” *Applied OPTICS*, 2000, vol 39, no 18, pp. 3023–3031.
- [16] T. Bifano et al., “Microelectromechanical deformable mirrors,” in *IEEE Journal of Selected Topics in Quantum Electronics*. 1999, vol. 5, no. 1, pp.83-89.
- [17] B. McComas and E. Friedman, “Field-balanced adaptive optics error functions for wide field-of-view space-based systems,” *Opt. Eng.*, 2002, vol. 41, no. 3, pp. 567–574.

INITIAL DISTRIBUTION LIST

1. Defense Technical Information Center
Ft. Belvoir, Virginia
2. Dudley Knox Library
Naval Postgraduate School
Monterey, California